J. Comp. App. Res. Mech. Eng. Vol. 11. No. 2, pp. 279-295, 2022 *DOI: 10.22061/JCARME.2021.6961.1906*

SRTTU

Journal of Computational and Applied Research in Mechanical Engineering

jcarme.sru.ac.ir

JCARME

ISSN: 2228-7922

Research paper

Numerical investigation of temperature effect on water hammer with cavitation in copper pipe rig

A. Saidani[a,*], A. Fourar[a] and F. Massouh[b]

[a]*Department of hydraulic, Faculty of technology, University of Batna 2 Mostafa Ben Boulaid, Batna 05000, Algeria*
[b]*Ecole nationale supérieure des arts et métiers, Paris, 75013, France*

Article info:

Article history:

Received:	10/06/2020
Revised:	13/07/2021
Accepted:	17/07/2021
Online:	19/07/2021

Keywords:

Hydraulic transient,
Water hammer,
Cavitation,
Column separation,
Unsteady flow.

[*]Corresponding author:
emirsaidani@gmail.com

Abstract

The paper investigates the temperature effect on water hammers in an isothermal pressurized copper pipe rig, for single and two-phase flows. The study concerns pressure wave's intensity, celerity, and attenuation. Also, the volume of cavities created during low-pressure periods is inspected. The mathematical model of hyperbolic equations is described by the dynamic and continuity equations, which have been transformed by the characteristics method into ordinary differential equations. Water hammer solver was built considering two different models of cavitation and column separation, the discrete vapor cavity model and the discrete gas cavity model. In addition to the quasi-steady friction model, two unsteady friction models were incorporated into the code, the convolution-based model proposed by Vardy and Brown and the instantaneous acceleration model proposed by Brunone. The simulations concern temperature range within 4°C to 95°C. Although the single and the two-phase water hammers don't behave in the same manner, the results obtained with the different models, show a significant influence of the temperature.

1. Introduction

All types of changes and disturbances of the steady flow regime generate pressure fluctuations, which means flow states that change through time; these states are called non-permanent or transient. Hydraulic transient in closed conduits or water hummer refers to pressure fluctuation caused by flow change depending upon the fluid involved [1]. It manifests itself as a wave's pressure surge generated from the perturbation source and propagates through the system.

Joukowsky [2] developed a formula of the velocity, also called the fundamental equation of water hammer, taking into account the compressibility of water and pipe elasticity using energy conservation principle and continuity equation. He studied wave reflections from an

open branch, the use of air chambers and surge tanks. Allievi [3, 4] developed a general theory of water hammers. He also produced charts for pressure rise at a valve due to uniform valve closure. Bergeron [5] also developed a graphical solution. It had some practical applications in pipe design before the advent of the computer. Streeter and Lai [6] developed a numerical model using a constant value of turbulent friction factor. Farther refinements to the governing equations of water hammers appeared later; their combined efforts have resulted in the classical mass and momentum equations for one-dimensional flow [7]. Actually, research is interesting for the transient phenomena behavior especially wave's form [8-10], frequency [11, 12] and reflection as well as attenuation [13-15]. The mathematical model, for one-dimensional water hummer flow, forms a set of two hyperbolic equations of momentum and continuity, which are quasi-linear, and hence the analytical or graphical solutions were not possible without particular simplifications. Therefore, numerical techniques are employed to approach the solutions. Various methods are available including finite difference (FD), finite volume (FV), and the most widely used method of characteristics (MOC) being accurate, stable, and simple to program on a computer.

Water hammer may be affected by many factors; therefore, the resolution models were extended with associated phenomena such as gas release, column separation, unsteady friction, viscoelastic pipe-wall behavior, and fluid-structure interaction [16]. However, system temperature, whether variable or constant, also affects fundamental properties such as density, viscosity, bulk modulus, vapor pressure, and pipe elasticity.

The current paper investigates the temperature effect on water hammers for single and two-phase flow cases. Thereby, the study is focused on wave speed, pressure head peaks, and attenuation at different temperatures and thus considering also cavities total volume and duration. For that reason, the experience performed by [17], consisting of a pressurized straight copper pipe-rig has been chosen as the reference problem since it has different velocities and Reynolds numbers.

The water hammer code was developed, for the simulation of different transient flow cases, by means of the Visual Basic Studio 2010. It includes solvers respectively of the single-phase model, the discrete vapor cavity model (DVCM) and the discrete gas cavity model (DGCM). In addition to the classical quasi-steady friction model, two unsteady friction models were incorporated, the convolution-based proposed by Vardy & Brown and the instantaneous acceleration proposed by Brunone.

The values of the fundamentals thermo-hydraulic water properties as density, dynamic viscosity, bulk modulus, and vapor pressure are obtained from the ASME Steam Tables Database which offers users access to water properties obtained from the IAPWS Industrial Formulation 1997 for the Thermodynamic Properties of Water and Steam [18].

The simulations were conducted respectively at 4°C, 10°C, 18.5°C, 20°C, 30°C, 40°C, 50°C, 53°C, 60°C, 70°C, 80°C, 90°C, and 95°C. However, results for both single and two-phase cases are presented at 4°C and 95°C, which present the lowest and highest temperatures, 18.5°C estimated experiment temperature and 53°C which provides the maximum wave speed. The frequency, pressure peak, and head dampening results are compared and discussed. Also, the cavitation inception, severity, and collapse are inspected.

2. Equations and units

2.1. Single-phase flow

The one-dimensional unsteady flow along the horizontal pipe is governed by differential equations; they are obtained by applying to an elementary portion of the pipeline two hyperbolic partial differential equations [1], the momentum equation and continuity equation, considering the compressibility of the water and the elasticity of the pipe. In the derivation of equations, the Reservoir-Pipe-Valve system is assumed isotherm, and the horizontal pipe has unique characteristics of the material, diameter, and wall thickness.

$$g\frac{\partial H}{\partial x}+\frac{1}{A}\frac{\partial Q}{\partial t}+J\ =\ 0 \tag{1}$$

$$g\frac{\partial H}{\partial t}+\frac{a^2}{A}\frac{\partial Q}{\partial x}=0 \quad (2)$$

where H is the piezometric head, Q is the volumetric flow rate, g is the gravitational acceleration, A is the cross-sectional area, x is the axial position, t is the time, J is the friction term. a is the wave speed, which includes the liquid compressibility, pipe elasticity, and wall constraint through the model by the following expression:

$$a=\frac{\sqrt{\frac{\beta}{\rho}}}{\sqrt{1+\left[\left(\frac{\beta}{E}\right)\left(\frac{D}{e}\right)c1\right]}} \quad (3)$$

where β is the bulk modulus of the liquid, ρ is the density of liquid, E is Young's modulus of elasticity of pipe-wall material, e is the pipe-wall thickness, D is the internal pipe diameter, $c1$ is the axial pipe-constraint parameter dependent on Poisson's ratio υ, and the relative wall thickness e/D.

In case of pipe anchored against axial movement $c1=1-\upsilon^2$ for thin wall $D/e>25$ and $c1=2e/D\ (1+\upsilon)+D(1-\upsilon^2)/D+e$ for thick wall $D/e<25$. [19]

Eqs. (1, 2) form a pair of quasi-linear hyperbolic partial differential equations. A general solution is not available. The standard procedure is the method of characteristics, unlike other methodologies based on finite difference or finite element, MOC is particularly suitable for systems with complex boundary conditions. It can easily model wave fronts generated by very fast transient flows and has the desirable attributes of accuracy, numerical efficiency, and programming simplicity [20]. The method consists in reducing the set of partial differential Eqs. (1, 2) to a family of ordinary differential equations so-called compatibility or characteristic equations.

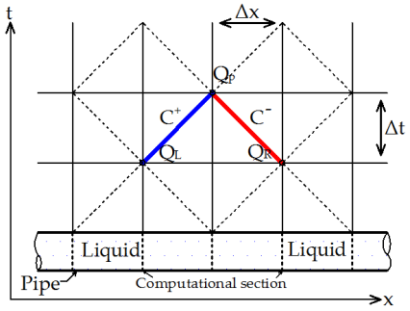

Fig. 1. Single-phase MOC grid in *x-t* plane.

So, along C^+ and C^-, as shown in Fig. 1, the compatibility equations are:

$$C^+:\begin{cases}\dfrac{dx}{dt}=+a\\ \dfrac{dQ}{dt}+\dfrac{gA}{a}\dfrac{dH}{dt}-AJ=0\end{cases} \quad (4)$$

$$C^-:\begin{cases}\dfrac{dx}{dt}=-a\\ \dfrac{dQ}{dt}-\dfrac{gA}{a}\dfrac{dH}{dt}+AJ=0\end{cases} \quad (5)$$

The resolution of these equations on the characteristics is done by integration or by the finite difference to find the global solution of the original problem on all the mesh. The solution can be integrated from the initial data; it looks for curves called characteristic curves or simply the characteristics along which the partial differential equation is reduced to a simple equation to solve. In this case, the characteristic curves are linear, since it is assumed that the wave speed is constant [21].

$$C^+:\ (H_P-H_L)+\frac{a}{gA}(Q_P-Q_L)+\frac{a\Delta t}{g}J_L=0 \quad (6)$$

$$C^-:\ (H_P-H_R)+\frac{a}{gA}(Q_R-Q_P)-\frac{a\Delta t}{g}J_R=0 \quad (7)$$

The solution consists of finding H and Q for each grid point along $t=\Delta t$ then proceeding to $t=2\Delta t$ until attain the desired time duration. Eqs. (6, 7) may be namely simplified as [19]:

$$H_P=C_P-BQ_P \quad (8)$$

$$H_P = C_m + BQ_P \quad (9)$$

in which $B = a/gA$, C_p and C_m are always known constants when equations are applied:

$$C_p = H_L + BQ_L - \frac{a\Delta t}{g}J_L \quad (10)$$

$$C_m = H_R - BQ_R + \frac{a\Delta t}{g}J_R \quad (11)$$

By first eliminating Q_P, in Eqs. (8, 9)

$$H_P = \frac{C_p + C_m}{2} \quad (12)$$

Then

$$Q_P = \frac{H_P - C_m}{B} \quad (13)$$

These Eqs. (12, 13) are valid for interior points. The initial condition must be specified for $t=0$, and boundary conditions must be imposed on the two points at either end $\forall t > 0$. The H_P and Q_P are respectively the unknown flow and the unknown piezometric head at point P at time $t+\Delta t$, Q_L and Q_R are the flow rates at neighboring sections of P at the previous time t, and H_L and H_R are the heads at neighboring sections of P at the previous time t.

Boundary conditions: At upstream, the reservoir is assumed to be infinite, hence, then the piezometric head remains constant during the short transient duration:

$$H_P = H_0 \quad (14)$$

and the flow rate is evaluated along the negative characteristics C^- as:

$$Q_P = Q_R + \frac{1}{B}(H_P - H_R) - A\Delta t J_R \quad (15)$$

At the downstream end, the valve closure behavior is expressed herein in terms of dimensionless time and approximating by Eq. (16):

$$\tau_v = 1 - \left(\frac{t}{t_c}\right)^m \quad (16)$$

where τ_v is the dimensionless valve closure time, t_c is the actual closure time, and t is the time. The m exponent in Eq. (16) is an adjustable constant determines the closing curve law and the polygonal approaching at true closing law, as shown in Fig. 2: m = 0 instantaneous closing, 0 <m< 1 concave closing, m = 1 linear closing, and 1 <m< ∞ convex closing [22].

The flow rate is evaluated by Eq. (17) [19]:

$$Q_P = -BC_v\sqrt{(BC_v)^2 - 2C_vC_p} \quad (17)$$

where

$$C_v = \frac{(Q_0\tau_v)^2}{2\,H_0} \quad (18)$$

and subscript $_0$ denotes the initial steady state.

The positive characteristic C^+ is used to calculate the head at the valve:

$$H_P = H_L - B(Q_P - Q_L) - \frac{a\Delta t}{g}J_L \quad (19)$$

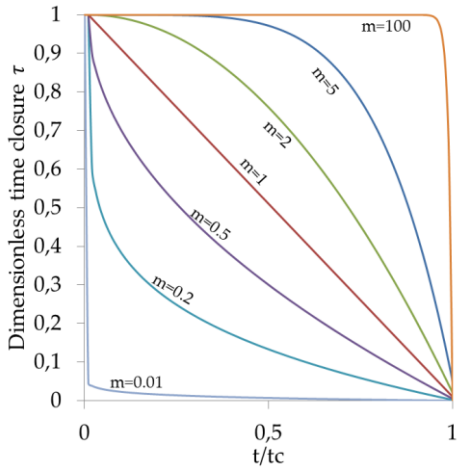

Fig. 2. Valve closure behavior.

2.2. Two phase flow (column separation and cavitation)

During the transient flow, pure liquid pressure can drop below vapor pressure which produces sudden appearance of cavities containing vapor, this is the basis of column separation regimes in which the liquid flow is completely separated by its vapor phase when the cavity is formed (Vapor cavitation). For Liquid containing solved gas if pressure falls below the saturation pressure but keeps above the liquid vapor pressure gas cavities increase their volume due to the pressure drop and dissolved gas is released (Gaseous cavitation). A subsequent increase in pressure will cause the bubbles to collapse [17]. A hydraulic transient model has been used in the simulation code by means of two approaches: DVCM and DGCM.

2.2.1. DVCM

If the pressure of the liquid is computed to be below the vapor pressure, cavities are allowed to form at grid points in the MOC, and pure liquid with a constant wave speed is assumed between two computational sections. The absolute pressure in a cavity is set equal to the vapor pressure $H_P=H_v$, and the cavity volume at the node is governed by the continuity Eq. (20):

$$V = \int_{t_{in}}^{t} (Q - Q_U)\partial t \tag{20}$$

In the MOC with staggered grid numerical integration of Eq. (20) is given as:

$$V_{cav\,P} = V_{cav\,P0} + 2\,\Delta t\big(\psi(Q_P - Q_{U\,P}) + (1-\psi)(Q_{P0} - Q_{U\,P0})\big) \tag{21}$$

where Q_U is the discharge upstream the node (inlet) and Q_P is the discharge at the downstream side (outlet), V_{cav} is the volume of the cavities, the subscript "$_P$" indicates points at time t, "$_{P0}$" indicates points at time t-2Δt, and ψ is a weighting factor, it is generally recommended to choose a value of ψ close to 0.5 to give the most accurate results [21].

It can be seen in Fig. 3 that there is a modification to the negative characteristics equation, C^-, since it departs from $Q_{U,B}$and not Q_B. Therefore the Q_B is replaced with $Q_{U,B}$ and $Q_{U,P}$ is calculated by Eq. (22):

$$Q_{U\,P} = \frac{C_p - H_P}{B} \tag{22}$$

Boundary Conditions: the head at the reservoir remains constant $H_P=H_0$, with $V_{cav}=0$, and always above the vapor pressure. At the downstream valve the discharge and the head are respectively evaluated with:

$$Q_{U\,P} = -BC_v\sqrt{BC_v{}^2 - 2C_vC_p} \tag{23}$$

$$H_P = C_p - BQ_{U\,P} \tag{24}$$

2.2.2. DGCM

As in DVCM, between each computational section and concentrated gas volume, pure liquid with a constant wave speed is assumed. Each isolated small volume of gas isothermally expands and contracts as the pressure varies, according to the perfect gas law [21].

$$m_gR_gT = P_g\alpha V = P_{g\,0}\alpha_0 V \tag{25}$$

in which V is the gas volume, $\alpha = V_g/V_m$ is the void fraction volume with V_g is the gas cavity volume, and V_m is the mixture volume, R_g is the gas constant, T is the temperature, P_g is the absolute partial pressure of the free gas, and m_g is the masse and assumed constant.

The DGCM is able to simulate vaporous cavitation by using a low initial gas void fraction $\alpha_0 \leq 10^{-7}$[17].

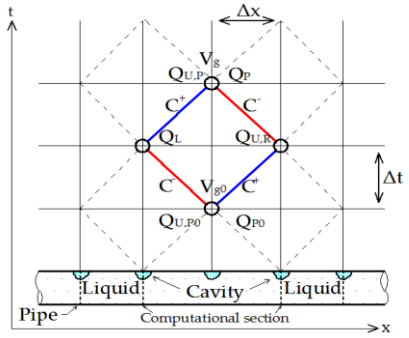

Fig. 3. Two-phase MOC grid in x-t plane.

Eq. (25) can be written in terms of head as:

$$(H_P - H_v)V_{g\,P} = (H_v - H_0)V_{g\,P0} \tag{26}$$

The volume of gas cavities is given by:

$$V_{g\,P} = V_{g\,P0} + 2\,\Delta t\left(\psi\left(\frac{H_P - C_m}{B} - \frac{C_p - H_P}{B}\right) + (1-\psi)(Q_{P0} - Q_{U\,P0})\right) \tag{27}$$

Eq. (26) can be written as:

$$V_{g\,P} = \frac{C_3}{(H_p - H_v)} \tag{28}$$

where

$$C_3 = \frac{P_{g,0}\alpha_0 V}{\rho_L g} \tag{29}$$

Eq. (27) can be rearranged into Eq. (30):

$$(H_P - H_v)^2 + 2B_1(H_P - H_v) - C_4 = 0 \tag{30}$$

Eq. (30) can be solved as a quadratic equation, and the head is calculated with Eq. (31):

$$H_P = \begin{cases} -B_1\left(1+\sqrt{1+B_B}\right) + H_v & if\ \ B_1 < 0\ and B_B > 0{,}001 \\ -B_1\left(1-\sqrt{1+B_B}\right) + H_v & if\ \ B_1 > 0\ and B_B > 0{,}001 \\ -2B_1 - \dfrac{C_4}{2B_1} + H_v & if\ \ B_1 < 0\ and B_B < 0{,}001 \\ \dfrac{C_4}{2B_1} + H_v & if\ \ B_1 > 0\ and B_B < 0{,}001 \\ \sqrt{C_4} + H_v & if\ \ B_1 = 0 \end{cases} \tag{31}$$

C_4, B_1, B_v, and B_B are defined as follows:

$$C_4 = \frac{B_2 B C_3}{\psi \Delta t} \tag{32}$$

$$B_1 = -B_2(C_p + C_m) + B_2 B B_v + \frac{H_v}{2} \tag{33}$$

$$B_v = \frac{\frac{V_{g\,P0}}{2\Delta t} + (1-\psi)(Q_{P0} - Q_{U\,P0})}{\psi} \tag{34}$$

$$B_B = \frac{C_4}{{B_1}^2} \tag{35}$$

where B_2=0.25, and the discharges Q_P and $Q_{U,P}$ are calculated by Eqs. (13, 17)

Boundary conditions: The upstream uses the same calculation method as for single phase flow the reservoir remains constant H_P=H_0. At the downstream valves, the discharge Q_U is similarly calculated by Eq. (23). However, the parameter B_2 is set to 0.5 to compute H_P.

2.3. Friction models

During the unsteady flow, the accurate evaluating of the hydraulic losses is essential to predict the wave's pressure propagation and attenuation. The friction forces are traditionally modeled with a constant friction factor or quasi-steady friction factor. Previous investigations showed that the models provide large discrepancies in attenuation, shape, and timing of pressure traces for high frequencies or high-velocity variation [23]. Therefore, the efforts of numerous researchers have resulted in developing miscellaneous methods to evaluate transient hydraulic losses with the unsteady friction models. Existing 1D models may be classified into three groups, namely those based on instantaneous acceleration, those using past velocities/accelerations, and those based on irreversible thermodynamics [24].

The friction term J is the sum of the quasi-steady J_q and unsteady J_u friction:

$$J = J_q + J_u \tag{36}$$

2.3.1. Quasi-steady friction

The quasi-steady friction term J_q is the skin friction of the pipe, it is modeled as:

$$J_q = \lambda \frac{Q|Q|}{2DA^2} \tag{37}$$

λ is the quasi-steady Darcy friction factor, which is updated for the local flow. In laminar flow regime (Re<2320), it is calculated using the Hagen-Poiseuille law:

$$\lambda = \frac{64}{Re} \tag{38}$$

The Colebrook-White iterative equation is used to obtain friction factor in the turbulent flow regime (Re> 2320).

$$\frac{1}{\sqrt{\lambda}} = -2\log\left(\frac{\varepsilon}{3{,}7D} + \frac{2{,}51}{Re\sqrt{\lambda}}\right) \tag{39}$$

The finite difference form of the Eq. (37) is written as:

$$C^+ : J_q = \left(\frac{\lambda}{2DA^2} Q_i^{j-1} \text{abs}\left(Q_i^{j-1}\right)\right) \tag{40}$$

$$C^- : J_q = \left(\frac{\lambda}{2DA^2} Q_i^{j+1} \text{abs}\left(Q_i^{j+1}\right)\right) \tag{41}$$

2.3.2. Unsteady friction

The unsteady friction term J_u is evaluated using both instantaneous acceleration and convolution-based friction models.

The Vitkovsky formulation of Brunone's model combines local inertia and wall friction unsteadiness. The description of the unsteady friction losses is proportional to the instantaneous local acceleration and instantaneous convective acceleration flow with a sign corrector [25]. It can be expressed as:

$$J_u = \frac{k}{A}\left(\frac{\partial Q}{\partial t} - a\text{sign}\,(Q)\frac{\partial Q}{\partial x}\right) \tag{42}$$

where

$$k = \frac{\sqrt{C^*}}{2} \tag{43}$$

C* Vardy's shear decay coefficient for the laminar flow regime is equal to 0.00476. However, for turbulent flow regime, C* is evaluated as follow:

$$C^* = \frac{7{,}41}{R_e^{\log\left(\frac{14{,}3}{R_e^{0{,}05}}\right)}} \tag{44}$$

In the MOC based on a rectangular grid, the finite difference approximation of Eq. (41) is given as follows:

$$C^+ : J_u = \frac{k}{A}\left(\frac{Q_{i-1}^{j-1} - Q_{i-1}^{j-2}}{\Delta t} - a\text{sign}\,(Q_{i-1}^{j-1})\ \text{abs}\left(\frac{Q_i^{j-1} - Q_{i-1}^{j-1}}{\Delta x}\right)\right) \tag{45}$$

$$C^- : J_u = \frac{k}{A}\left(\frac{Q_{i+1}^{j-1} - Q_{i+1}^{j-2}}{\Delta t} - a\text{sign}(Q_{i+1}^{j-1})\ \text{abs}\left(\frac{Q_{i+1}^{j-1} - Q_i^{j-1}}{\Delta x}\right)\right) \tag{46}$$

The role of the proportionality coefficient, k, is crucial for this model. This coefficient may be assumed constant with the value fitted to conform with computational and experimental results or depending on the initial Re value or as a variable, depending on the instantaneous Re values during unsteady flow [26].

The Vardy and Brown's model is based on the convolution of past fluid accelerations and a weighting function. It follows from an analysis

of axisymmetric flow separated into two layers according to the empirical distribution of turbulent viscosity coefficient two layers model [24].

$$J_u = \frac{16\,\mu}{\rho D^2 A}\left(\frac{\partial Q}{\partial t} * W(\tau)\right) \tag{47}$$

where

$$\tau = \frac{4\,\rho t}{\mu D^2} \tag{48}$$

The Vardy and Brown weighting function is formulated as below:

$$W(\tau) = \frac{A^* \tau^{B^*}}{\sqrt{\tau}} \tag{49}$$

where:

$$A^* = \frac{1}{2\sqrt{\pi}},\ B^* = \frac{R_e^k}{12{,}86},\ k = \log\left(\frac{15{,}29}{R_e^{0{,}0567}}\right)$$

Eq. (47) is approximated with first-order finite-difference as follows:

$$C^+ : J_u = \frac{16\,\mu}{\rho D^2 A}\sum_{J=1}^{n-1}\left(\frac{Q_{i-1}^{j+1} - Q_{i-1}^{j}}{\Delta t}, W\left((n - j)\Delta\tau - \frac{\Delta\tau}{2}\right)\right) \tag{50}$$

$$C^- : J_u = \frac{16\,\mu}{\rho D^2 A}\sum_{J=1}^{n-1}\left(\frac{Q_{i+1}^{j+1} - Q_{i+1}^{j}}{\Delta t}, W\left((n - j)\Delta\tau - \frac{\Delta\tau}{2}\right)\right) \tag{51}$$

3. Reference problem

As shown in Fig. 4, the system consists of a hydro-pneumatic tank at the upstream end supplied by a centrifugal pump with a nominal flow rate of 1 l/s, a nominal head of 46 m, a 15.22 m horizontal straight copper pipe with an inner diameter of 0.02 m and wall thickness of 0.001 m and two quarter turn ball valve ball valves at the downstream end of a pneumatically actuated used for generating the water hammer, and a manually operated used to control the initial discharge.

Two experiments were conducted by Soares et al [17]. The first one with a low initial velocity of 0.423 m/s resulted in a single-phase water hammer, whereas the second one with the largest initial velocity of 0.497 m/s resulted in a two-phase water hammer. Fig. 5 shows the pressure traces for single-phase flow (initial discharge, Q_0 = 0.133 l/s) as well as the transient pressure data for two-phase flow (initial discharge, Q_0 = 0.156 l/s) acquired by the transducer T1 at the valve.

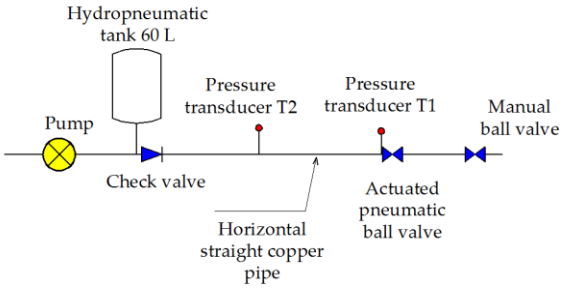

Fig. 4. Experiment system.

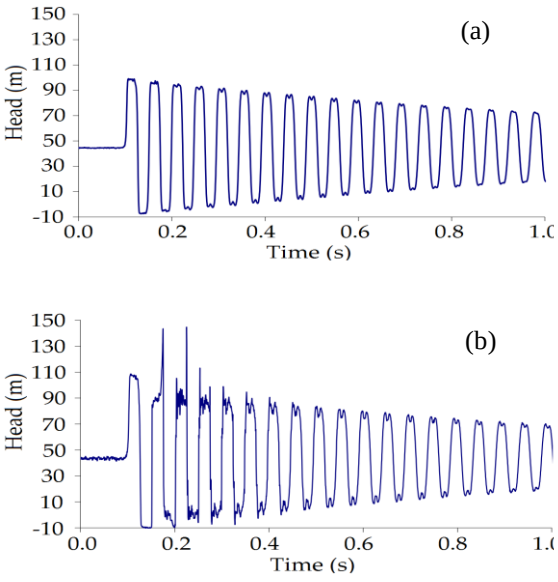

Fig. 5. Experiment pressure traces at the valve; (a) single-phase flow and (b) two-phase flow.

4. Results and discussion

4.1. Steady-state

For the steady-state, the discharge through the pipe remains constant, whereas the pressure head drops along the pipe by the fact of the friction. The results for the steady state over the temperature range are given in Table 1:

The pressure head at the valve, for the two cases increases with temperature as shown in Fig. 6.

The maximum pressure head at the valve is obtained at 95°C for the two cases, this is due to the fact that pressure head attenuation ΔH (expressed in percent %), caused by the viscous forces, is less as the temperature increases.

4.2. Transient state

For the simulation of the transient flow, the MOC grid is set with a number of 48 reaches. The closure time of the valve was not described by Soares et al., and therefore it is estimated at 18 ms, the time it takes to reach maximum pressure from steady-state pressure [21], m is chosen as 5, which is the best fit for the valve closure (Fig. 7).

The wave speed value depends on the compressibility of the liquid, which has a maximum value at 50°C (Fig. 8). It is thus affected by the pressure, temperature, and gas content of the liquid, as well as the pipe elasticity. However, in this paper, only temperature and pipe elasticity are considered.

Table 1. The steady-state results for the cases 1 and 2 at the valve.

T (°C)	Case1			Case2		
	Q (l/s)	H (m)	ΔH (%)	Q (l/s)	H (m)	ΔH (%)
4	0.133	45.745	23.758	0.156	45.664	23.894
10	0.133	45.758	23.737	0.156	45.680	23.866
18.5	0.133	45.772	23.713	0.156	45.699	23.835
20	0.133	45.775	23.709	0.156	45.702	23.830
30	0.133	45.788	23.687	0.156	45.719	23.802
40	0.133	45.798	23.670	0.156	45.732	23.779
50	0.133	45.807	23.758	0.156	45.744	23.761
53	0.133	45.809	23.737	0.156	45.747	23.756
60	0.133	45.814	23.713	0.156	45.753	23.745
70	0.133	45.820	23.709	0.156	45.761	23.732
80	0.133	45.825	23.687	0.156	45.768	23.720
90	0.133	45.830	23.670	0,156	45.774	23.710
95	0.133	45.832	23.655	0.156	45.776	23.706

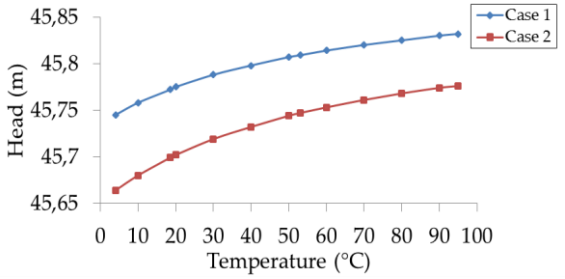

Fig. 6. Temperature effect on the pressure head at the valve for the steady state.

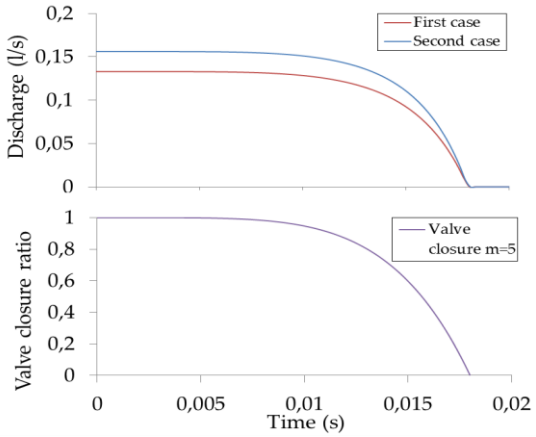

Fig. 7. Discharges at the downstream end during valve closure.

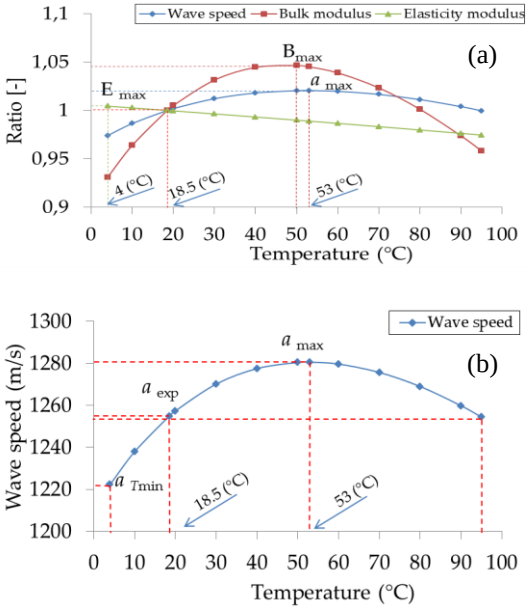

Fig. 8. Temperature effect on the wave speed; (a) ratios of a, B, and E to those at 18.5°C and (b) the wave speed behavior within the temperature range.

The elasticity modulus of copper is assumed to be a function of the temperature and modeled as polynomial curve fits of temperature [27] as follow:

$$E_{Copper} = (a \cdot ((T \cdot 9/5) + 32)^2 + ((b \cdot ((T \cdot 9/5) + 32) + c)) \cdot d \quad (52)$$

where

$$a=-1.464828,\ b=-2578{,}234$$
$$c=16233170\ \ d=6894.757$$

As shown in Fig. 8, a minimal wave speed value is obtained at the lowest temperature of 4°C. After that, it increases with temperature until it reaches a maximum value of 1280.55 m/s at 53 °C. However, since the ambient temperature of the experiment was not given by Soares et al. [17], it is estimated from the wave speed curve, which corresponds to 18.5°C at 1255m/s.

4.2.1. First case

With initial discharge Q_0=0.113l/s, a comparison at the valve, between the experimental data and computational results at 18.5°C, for the single phase is represented in Fig. 9.

The quasi-steady friction model correctly estimates the peak in the first pressure zone but does not accurately describe the attenuation of the pressure head. However, no offset between the experimental data and the computational results with unsteady friction models is expected.

As shown in Fig. 10, the computational results for the initial case are given for each significant temperature. The pressure head traces represent a notable shift in phase and attenuation, increasing in time.

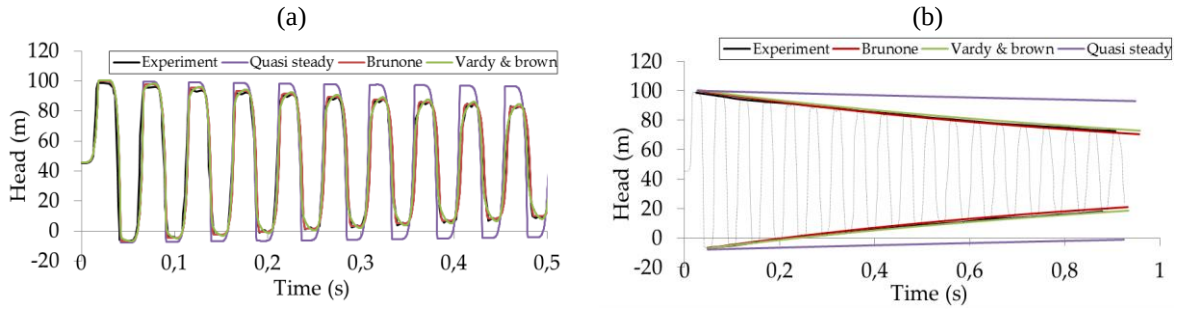

Fig. 9. Comparison between experiment and single-phase results at 18.5°C; (a) pressure traces and (b) head dampening.

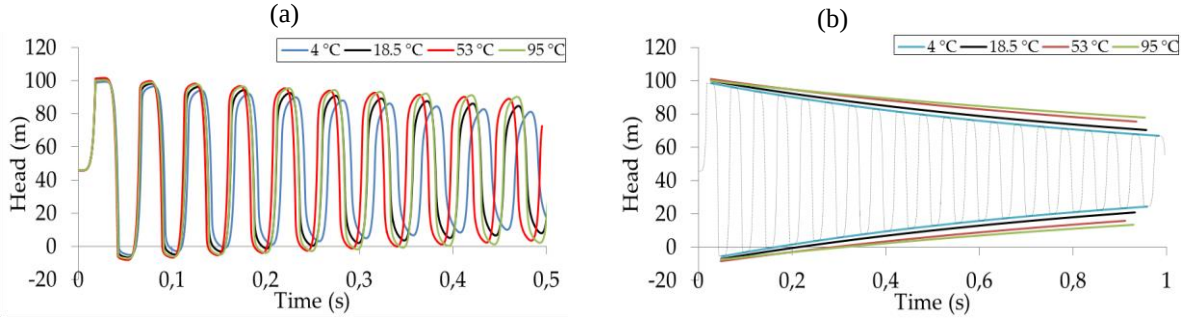

Fig. 10. The single-phase results for 4°C, 18.5°C, 53°C, and 95°C; (a) pressure traces and (b) head dampening.

Table 2 reports values of wave speed, oscillation frequency, first and tenth pressure zone peaks, and their deviations from those at 18.5°C. As well as, the attenuation ratio of the tenth pressure zone peak. The lowest values of the wave speed (-2.6%) and frequency are obtained at 4°C. Thus providing the minimum first pressure zone peak (-1.43%). However, at this temperature, the largest attenuation of pressure head (-19.17%) is obtained at the tenth pressure zone. On the other hand, the maximum values of wave speed (+2%), frequency, and first pressure zone peak (+1.112%) are reached at 53°C. On the other hand, at 95°C, values have not many deviations excepting the smaller attenuation ratio (-12.1%) resulting, consequently, in the most important peak in the tenth pressure zone.

4.2.2. Second case

In the second case, the initial discharge Q_0=0.156 l/s resulted in two-phase transient flow. The MOC is set up with a low free gas void fraction α of 10^{-7}. A weighting factor ψ of 0.55 for both DVCM and DGCM; however, at temperatures greater than 53°C, DGCM requires higher values of ψ to minimize excessive numerical oscillations, see Table 3.

Fig. 11 shows the comparison between the experimental data and computational results obtained for 18.5°C, at the valve, with DVCM and DGCM combining the unsteady friction models. It can be seen no offset at the first pressure zone and a good agreement in the second one, where the highest pressure peaks are caused by the implosion of bubbles created during low pressure periods. However, neither of the models is able to reproduce the intense pressure peak at the third pressure zone.

Values of wave speed, oscillation frequency, as well as max and min pressure heads in the first, second, and third pressure zone, within the temperature range, are summarized in Table 4 and Table 5.

Table 3. Weighting factor ψ chosen for DVCM and DGCM.

T (°C)	DVCM	DGCM
$4 \leq T < 53$	0.55	0.55
$53 \leq T < 80$	0.55	0.65
$80 \leq T \leq 95$	0.55	0.80

Table 2. The single-phase results for 4°C, 18.5°C, 53°C, and 95°C.

T (°C)	Wave speed (m/s)	Frequency (Hz)	Deviation (%)	First pressure zone (m)	Deviation (%)	Tenth pressure zone (m)	ΔH (%)
4	1222.28	20.08	-2.600	98.642	-1.430	79.73	-19.17
18.5	1254.89	20.61	-	100.073	-	82.86	-17.20
53	1280.55	21.03	+2.045	101.186	+1.112	86.83	-14.19
95	1254.51	20.60	-0.030	100.074	+0.001	87.97	-12.10

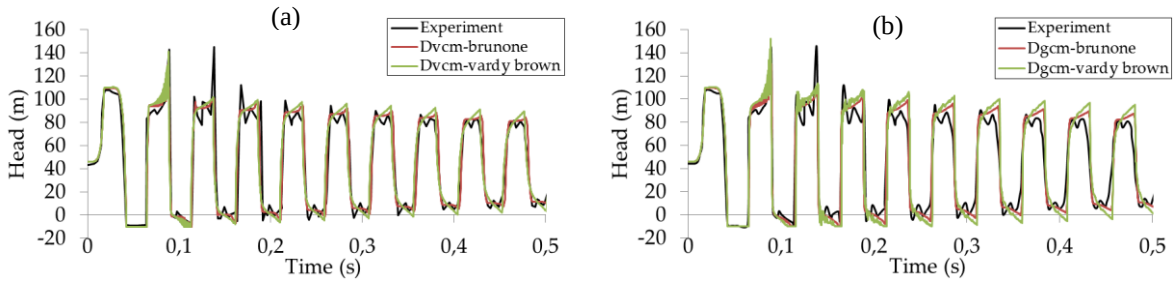

Fig. 11. Comparison between experiment and two-phase results at 18.5°C; (a) DVCM with unsteady friction models and (b) DGCM with unsteady friction models.

Table 4. The DVCM with unsteady friction models results for H_{max} and H_{min} at 4°C, 18.5°C, 53°C, and 95°C in the first, second, and third pressure zone compared to the experiment for the second case.

T (°C)	Wave speed (m/s)	Frequency (Hz)	Peak	First pressure zone		Second pressure zone		Third pressure zone	
				Brunone	V&B	Brunone	V&B	Brunone	V&B
4	1222.28	20.08	H_{max}	107.83	108.72	118.62	124.30	100.75	101.84
			H_{min}	-10.26	-10.26	-10.26	-10.26	-10.26	-10.26
18.5	1254.89	20.61	H_{max}	109.51	110.22	136.50	141.01	100.24	101.39
			H_{min}	-10.14	-10.14	-10.14	-10.14	-10.14	-10.14
53	1280.55	21.03	H_{max}	110.82	111.33	135.89	170.81	99.39	100.17
			H_{min}	-9.00	-9.00	-9.00	-9.00	-9.00	-9.00
95	1254.51	20.60	H_{max}	109.52	109.90	168.51	170.24	101.10	98.36
			H_{min}	-1.77	-1.77	-1.77	-1.77	-1.77	-1.77
Experiment	1255	20.61	H_{max}	108.47		143.70		144.85	
			H_{min}	-10.07		-9.82		-6.34	

Table 5. The DGCM with unsteady friction models results for H_{max} and H_{min} at 4°C, 18.5°C, 53°C, and 95°C in the first, second, and third pressure zone compared to the experiment for the second case.

T (°C)	Wave speed (m/s)	Frequency (Hz)	Peak	First pressure zone		Second pressure zone		Third pressure zone	
				Brunone	V&B	Brunone	V&B	Brunone	V&B
4	1222.28	20.08	H_{max}	107.82	108.72	112.51	115.59	103.49	109.92
			H_{min}	-10.24	-10.13	-10.24	-10.19	-10.02	-10.17
18.5	1254.89	20.61	H_{max}	109.51	110.21	132.94	154.52	104.39	121.42
			H_{min}	-10.13	-10.11	-10.13	-10.12	-9.97	-10.12
53	1280.55	21.03	H_{max}	110.82	111.32	146.50	169.55	112.11	116.54
			H_{min}	-9.00	-9.00	-9.00	-9.00	-8.95	-8.98
95	1254.51	20.60	H_{max}	109.51	109.89	165.85	169.68	132.20	140.54
			H_{min}	-1.78	-1.78	-1.78	-1.78	-1.76	-1.77
Experiment	1255	20.61	H_{max}	108.47		143.70		144.85	
			H_{min}	-10.07		-9.82		-6.34	

The same values of wave speed and frequency are obtained, as in the single phase case, because it is assumed in DVCM and DGCM that cavities are confined to computational sections, and wave speed remains constant. Although the highest pressure peaks in the first pressure zone are obtained at 53°C, the maximum peaks over all pressure zones are reached in the second pressure zone at 95°C for the two-phase flow, and that is unlike the single phase case where the 53°C gives usually the maximum peaks only in the first pressure zone. This may be explained by the fact of cavities collapsing and columns rejoining in the first pressure zone, thus providing the intense pressure peaks in the second pressure zone. On the other hand, it is noted that in all pressure zones, minimum peaks are obtained at 4°C.

The pressure traces for 4°C, 18.5°C, 53°C, and 95°C, are exposed in Fig. 12. The same as in the single-phase case, it can be seen that for all combinations, the pressure traces represent a notable shift in phase and attenuation, increasing in time.

Short-duration pressure peaks in the second and third pressure zones, resulting from cavities collapse, are more intense at higher temperatures. The wave's magnitude decreases considerably since the attenuations of pressure peaks H_{max} and H_{min} are mostly intense at 95°C, as shown in Table 6.

We note that mush dissipation for transient flow at higher temperatures We note that at higher temperatures, the transient flow is more dissipative. This is due to the fact that the cavitation and column separation severity are dependent on temperature.

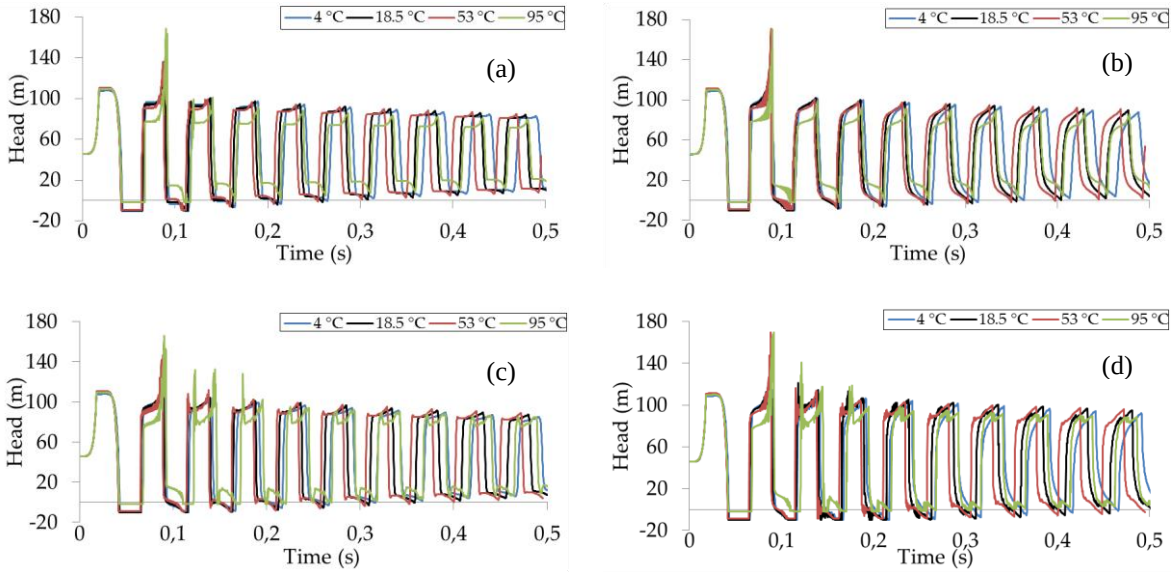

Fig. 12. The two-phase results for 4°C, 18.5°C, 53°C, and 95°C; (a) DVCM-Brunone, (b) DVCM-Vardy and Brown, (c) DGCM-Brunone, and (d) DGCM-Vardy and Brown.

Table 6. First pressure zone peaks deviations from experiment and attenuation ratios ΔH (%) at tenth pressure zone by DVCM and DGCM with unsteady friction models at 4°C, 18.5°C, 53°C, and 95°C.

T (°C)	Peak	DVCM				DGCM			
		Deviation (%)		ΔH (%)		Deviation (%)		ΔH (%)	
		Brunone	V&B	Brunone	V&B	Brunone	V&B	Brunone	V&B
4	H_{max}	-0.06	+0.66	-23.41	-19.56	-0.06	+0.77	-21.13	-15.16
	H_{min}	+9.38	+9.38	-182.36	-135.86	+9.16	+8.00	-158.30	-87.76
18.5	H_{max}	+1.56	+2.06	-23.24	-18.23	+1.50	+2.15	-20.36	-13.70
	H_{min}	+8.10	+8.10	-169.13	-117.06	+8.10	+7.78	-137.48	-61.72
53	H_{max}	+2.72	+3.08	-23.30	-18.32	+2.72	+3.18	-19.60	-14.00
	H_{min}	-4.05	-4.05	-168.67	-105.78	-4.05	-4.05	-122.22	-52.89
95	H_{max}	+1.51	+1.76	-27.07	-21.78	+1.50	+1.85	-20.99	-18.47
	H_{min}	-81.1	-81.1	-762.71	-415.82	-81.02	-81.02	-457.87	-266.85
Experiment	H_{max}	-		-24.63		-		-24.63	
	H_{min}	-		-176.55		-		-176.55	

The total volume of vapor and gas cavities at the valve for 4°C, 18.5°C, 53°C, and 95 °C with both DVCM and DGCM in a combination of unsteady friction models, during the pressure drop periods, are shown in Fig. 13.

As shown in Fig. 13, the largest total cavities for all temperatures are formed in the first pressure zone, once the negative wave resulting from the reverse reaches the vapor pressure at the valve. It can be seen that the total cavity volumes obtained with both DVCM and DGCM are closer to each other when the same friction model is used. However, an important divergence between the results obtained with the two unsteady friction models employed. The results for the total cavities volume and duration, within the temperature range are summarized in Table 7 and presented in Fig. 14.

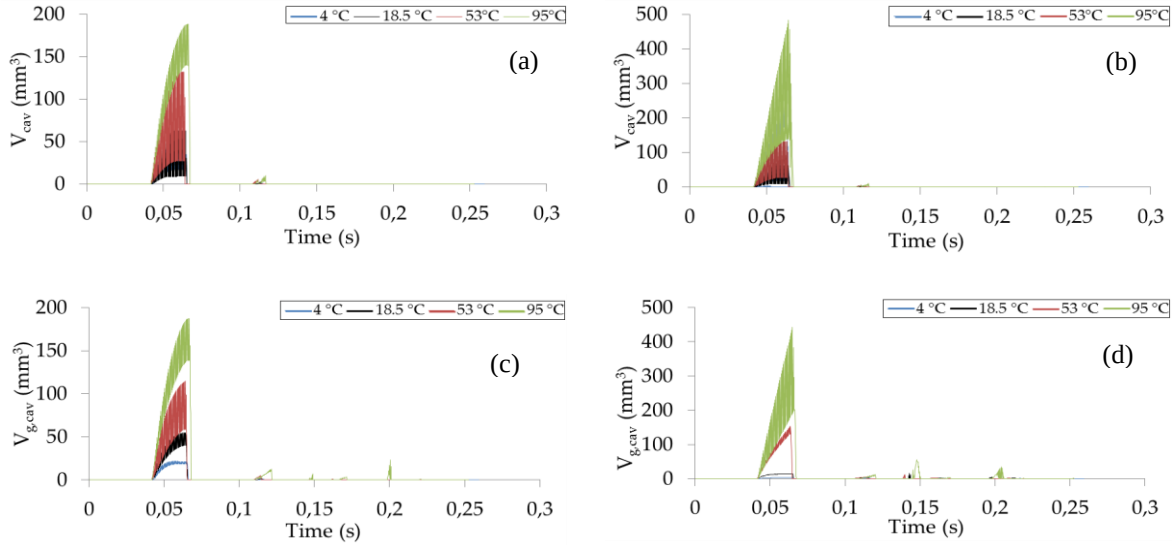

Fig. 13. Total cavity volume at the valve for 4°C, 18.5°C, 53°C, and 95°C; (a) DVCM-Brunone, (b) DVCM-Vardy and Brown, (c) DGCM-Brunone, and (d) DGCM-Vardy and Brown.

Table 7. Total volume and duration of cavities obtained at the valve within temperature range with both DVCM and DGCM in combination of unsteady friction models.

T (°C)	DVCM				DGCM			
	V & B		Brunone		V & B		Brunone	
	$V_{Tot.cav}$ (mm)	Duration (s)	$V_{Tot.cav}$ (mm)	Duration (s)	$V_{Tot.g.cav}$ (mm)	Duration (s)	$V_{Tot.g.cav}$ (mm)	Duration (s)
4	3.54	0,013490	52.39	0,021532	4.26	0,020235	21.65	0,021013
10	21.52	0,022029	51.68	0,022029	7.25	0,022029	34.38	0,021517
18.5	96.23	0,021983	63.16	0,022236	15.98	0,022741	54.85	0,022236
20	104.92	0,021940	64.67	0,021688	17.72	0,022697	56.44	0,022192
30	148.96	0,021719	124.39	0,022219	55.56	0,022718	81.80	0,022219
40	190.75	0,022339	106.59	0,022090	94.66	0,022587	92.45	0,022090
50	235.25	0,022783	120.47	0,022535	136.43	0,023030	108.47	0,022288
53	249.34	0,022781	132.19	0,022038	153.07	0,023028	114.65	0,022533
60	278.77	0,022301	184.09	0,022549	186.85	0,023045	131.02	0,022549
70	344.87	0,022122	124.75	0,023117	241.87	0,023365	122.98	0,022868
80	397.08	0,023489	237.66	0,023239	317.08	0,023739	186.31	0,023989
90	413.52	0,023911	190.92	0,024162	374.99	0,024666	183.91	0,024162
95	483.86	0,023761	188.28	0,025025	442.25	0,025278	187.51	0,025025

Significant discrepancies between the total cavities volume obtained with the two unsteady friction models. Using Vardy and Brown's model gives much higher values than Brunone's model, respectively about 400% compared to 200% of total cavities volume increase at 95°C with the two unsteady friction models.

As shown in Fig. 14, although discrepancies are considerable between unsteady friction models results, it is noted that the total cavities volume at the valve increases as temperature for both DVCM and DGCM increases. Maximum total cavities volumes are reached at 95°C.

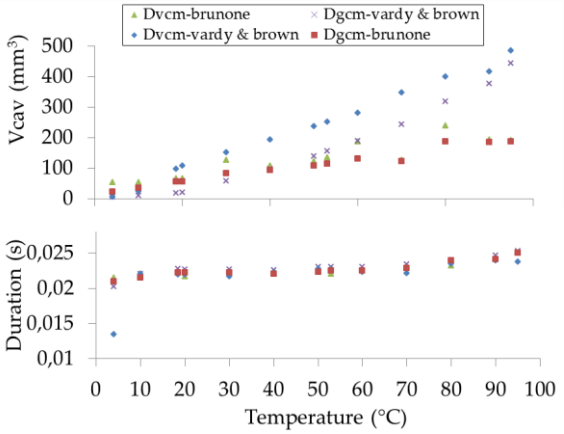

Fig. 14. Effect of the temperature on the cavities volume and duration.

However, DVCM in combination with Vardy and Brown's model gives respectively around 2, 5, and 136 times total cavity volumes obtained at 4°C, 18.5°C, and 53°C.

On the other side, the existence duration of cavities, from the first inception until collapse, shows an important dependence on temperature. The time of existence is maximal for 95°C with all models combinations. Compared to the durations obtained for 4°C, using DVCM with unsteady friction Vardy and Brown's model, gives about 10 ms (76%), 1.8 ms(47%), and 0.9 ms (45%) of increase, respectively for 95°C, 53°C, and 18.5°C.

5. Conclusions

The paper presents a numerical investigation of the temperature influence on water hammers with cavitation. The reference problem performed by Soares et al., supposed to be isothermal during the simulation, consists of a pressurized straight copper pipe rig and has been chosen to analyze two water hammer cases, single- and two-phase transient flow since the experiment had different discharges.

The water hammer solver was developed for single- and two-phase flow simulation using the discrete vapor cavity model DVCM and the discrete gas cavity model DGCM. Two unsteady friction models were incorporated, in addition to the quasi-steady friction model, the convolution-based proposed by Vardy and Brown and the instantaneous acceleration proposed by Brunone.

A total of 196 simulations was conducted for the two transient flow cases, respectively at 4, 10°C, 18.5°C, 20°C, 30°C, 40°C, 50°C, 53°C, 60°C, 70°C, 80°C, 90°C, and 95°C, using single-phase model, DVCM and DGCM in a combination of all friction models. The results are discussed for the significant temperatures of 4°C and 95°C, corresponding to the lowest and the highest temperatures, 18.5°C the estimated experiment temperature and 53°C, which gives the maximal wave speed. Discussion concerns wave speed, pressure peaks intensity, and pressure head attenuation. Also, cavity total volume and duration are reported.

Just before water hammer was triggered, at the steady-state regime, temperature acted on the permanent flow by reducing head losses due to friction. Permanent flow at higher temperatures conserves more hydraulic energy than at low temperatures. This is due to the viscosity dependence on the temperature, and therefore, the highest pressure heads at the valve were obtained for 95°C.

During the water hammer, at the unsteady regime, the temperature acted differently on the transient flow. In single- and two-phase transient flow, wave speed and attenuation are temperature dependants at the same time.

Unlike permanent flow in which viscosity is the unique parameter in consideration, the bulk modulus is a primordial factor, depending upon the temperature in the transient flow, and has a direct impact on the wave's amplitude and frequency. In the case of unsteady flow, pressure head magnitude is affected by temperature via the bulk modulus in addition to viscosity which its effect is limited in the attenuation. Contrary

to viscosity behavior, bulk modulus increases with temperature until it reaches a maximum value at around 50°C, then it decreases. Thereby, the single-phase water hammer is mostly brutal around this temperature and follows practically the same path as the bulk modulus. However, vapor pressure is another parameter taking place in the two-phase transient flow, depending also upon temperature. It is in the origin of cavities inception, has a considerable increase with temperature, and influence greatly on the severity of cavitations (total volume and time of existence), which provoke intense pressure peaks of court duration, after their collapse, appearing from the second pressure zone. Short duration pressure peaks are more intense after the first pressure zone and increases greatly with temperature until they become mostly brutal at 95°C, and hydraulic energy dissipates significantly in the two phase transient flow for higher temperatures conversely to the single-phase.

The water hammer is considerably sensitive to the system temperature. Therefore, it must be considered in the conception and design of hydraulic systems, especially those operating under different thermal conditions. However, since the discrepancies increases between results obtained with different models combinations, it seems that additional improvements are needed to water hammer with cavitation and unsteady friction models for best predictions at a higher temperature.

References

[1] M. H. Chaudhry, *Applied Hydraulic Transients*,1st ed. Van nostrand reinhold company, New York, pp. 27-73, (1979).

[2] N. E. Joukowski, "Memoirs of the imperial academy society of saint petersburg", *Proc. Amer. Water Works Assoc*. Vol. 24, No. 1, pp. 341–424, (1898).

[3] L. Allievi, "Teoria generale del moto perturbato dell'acqua ni tubi in pressione", *Ann. Soc. Ing. Arch. Ithaliana*, Vol. 17, No. 5, pp. 285-325, (1902).

[4] L. Allievi, "Teoria del colpo d'ariete", *Atti Coll. Ing. Arch. Italiani*, Vol. 46, No. 1, pp. 336-373. (1913).

[5] L. Bergeron, "Etude des variations de régime dans conduits d'eau", *Rev. Gen. Hydraul*., Vol. 1, No. 1, pp.12-69, (1935).

[6] V. L. Streeter and C. Lai, "Water hammers analysis including fluid friction", *Trans. Amer. Soc. Civ. Eng*., Vol. 128, No.1, pp.1491–1524, (1963).

[7] M. S. Ghidaoui, M. Zhao, D. A. McInnis and D. H. Axworthy, "A review of water hammer theory and practice", *J. Appl. Mech. Rev*., Vol. 58, No. 1, pp.49–76, (2005).

[8] A. Tijsselinga, M. Lambertb, A. Simpsonb, M. Stephensb, J. Vitkovsky and A. Bergant, "Skalak's extended theory of water hammer", *J. Sound Vib*., Vol. 310, No. 3, pp. 718–728, (2008).

[9] S. Meniconi, B. Brunone and M. Ferrante, "In-line pipe device checking by short period analysis of transient tests", *J. Hydraul. Eng*., Vol. 137, No. 7, pp. 713–722, (2011).

[10] S. Meniconi, B. Brunone, M. Ferrante and C. Massari, "Small amplitude sharp pressure waves to diagnose pipe systems", *J. Water Res. Man*., Vol. 25, No. 1, pp. 79–96, (2011).

[11] M. Meniconi, H. Duan, P. Lee, B. Brunone, M. Ghidaoui and M. Ferrante, "Experimental investigation of coupled frequency-and time-domain transient test-based techniques for partial blockage detection in pipelines", *J. Hydraul. Eng*., Vol. 139, No. 10, pp.1033–1040, (2013).

[12] P. Lee, H. Duan, M. S. Ghidaoui and B. Karney, "Frequency domain analysis of pipe fluid transient behavior", *J. Hydraul. Res*., Vol. 51, No.6, pp. 609–622, (2013).

[13] M. Siamao, "Mechanical interaction in pressurized pipe systems", *J. Water*, Vol. 7, No. 11, pp. 6321-6350, (2015).

[14] S. Elaoud and E. Hadj-Taïeb, "Influence of pump starting times on transient flows in pipes", *J. Nuclear. Eng. Des*., Vol. 241, No. 9, pp. 3624-3631, (2011).

[15] F. Duan, J. Lee and S. Ghidaoui, "Transient wave-blockage interaction in pressurized water pipelines", *J. Proc. Eng*., Vol.70, No. 1, pp. 573-582, (2014).
[16] Q. Hou, H. Kruisbrink, S. Tijsseling and A. Keramat, "Simulating water hammer with corrective smoothed particle method", *Technische Universiteit Eindhoven (Casa Report)*, Vol.1214, No. 1, pp. 16, (2012).
[17] K. Soares, N. Martins and I. Covas, "Investigation of transient vaporous cavitation: experimental and numerical analyses", *J. Proc. Eng*., Vol. 119, No. 1, pp. 235–242, (2015).
[18] A. Harvey, W. Parry, J. Belows, J. Gallagher and R. Harwood, *ASME international steam tables for industrial use*, ASME Press, Amer. Soc. Mech. Eng., (2014).
[19] E. B. Wylie, V. L. Streeter and L. Suo, *Fluid Transients in Systems*. Prentice hall: Englewood cliffs, New York, (1993).
[20] J. Twyman, "Speed calculation for water hammer analysis", *Obras. Proyectos*., Vol. 20, No. 1, pp. 86-92, (2016).
[21] J. Rune Larsen, J. Lassen and K. Mando, Matthias and Andreasen, "Implementation and validation of a free open source 1d water hammer code", *J. Fluid*, Vol. 3, No. 1, pp. 64, (2018).
[22] G. Provenzano, F. Baroni and J. Aguerre, "The closing function in the water hammer modeling", *Lat. Amer. App. Res.*, Vol. 41, No. 1, pp. 43-47, (2011).
[23] K. Urbanowicz and Z. Zarzycki, "Convolution integral in transient pipe flow", *J. Task Quart.*, Vol. 16, No. 3, pp. 277–291, (2012).
[24] E. Vardy and B. Brown, "Transient turbulent friction in smooth pipe flows", *J. Sound Vib*., Vol. 259, No. 1, pp. 1011–1036, (2003).
[25] A. Bergant, A. Simpson and J. Vítkovský, "Developments in unsteady pipe flow friction modeling", *J. Hydraul. Res*., Vol. 39, No. 1, pp. 249–257, (2001).
[26] A. Adamkowski, Adam and M. Lewandowski, "Experimental examination of unsteady friction models for transient pipe flow", *J. Fluid Eng*., Vol. 128, No. 6, pp.1351, (2006).
[27] Engineering Toolbox, *Young's modulus of elasticity for metals and alloys*, (2004).

How to cite this paper:

A. Saidani, A. Fourar and F. Massouh, "Numerical investigation of temperature effect on water hammer with cavitation in copper pipe rig", *J. Comput. Appl. Res. Mech. Eng.*, Vol. 11, No. 2, pp. 279-295, (2022).

DOI: 10.22061/JCARME.2021.6961.1906

URL: https://jcarme.sru.ac.ir/?_action=showPDF&article=1576